HAL
open science

High order fluid structure interaction in 2D and 3D: Application to blood flow in arteries

Christophe Prud'Homme, Gonçalo Pena, Vincent Chabannes

To cite this version:

Christophe Prud'Homme, Gonçalo Pena, Vincent Chabannes. High order fluid structure interaction in 2D and 3D: Application to blood flow in arteries. ACOMEN 11 - 5th International Conference on Advanced COmputational Methods in ENgineering, Nov 2011, Liège, Belgium. pp.1-10. hal-00657154

HAL Id: hal-00657154

https://hal.science/hal-00657154v1

Submitted on 6 Jan 2012

HAL is a multi-disciplinary open access archive for the deposit and dissemination of scientific research documents, whether they are published or not. The documents may come from teaching and research institutions in France or abroad, or from public or private research centers.

L'archive ouverte pluridisciplinaire **HAL**, est destinée au dépôt et à la diffusion de documents scientifiques de niveau recherche, publiés ou non, émanant des établissements d'enseignement et de recherche français ou étrangers, des laboratoires publics ou privés.

Fifth International Conference on Advanced COmputational Methods in ENgineering (ACOMEN 2011)
Liège, Belgium, 14-17 November 2011
(c)University of Liège, 2011

High order fluid structure interaction in 2D and 3D Application to blood flow in arteries

V. Chabannes[1], G. Pena[2] and C. Prud'homme[1]

[1] Université Grenoble 1 / CNRS, Laboratoire Jean Kuntzman / UMR 5224.
Grenoble, F-38041, France

[2] CMUC, University of Coimbra
Largo D. Dinis, Apartado 3008, 3001-454 Coimbra, Portugal

e-mails: {*vincent.chabannes,christophe.prudhomme*}*@imag.fr*, *gpena@mat.uc.pt*

Abstract

Accuracy is critical if we are to trust the simulation's predictions. In settings such as fluid-structure interaction it is all the more important to obtain reliable results to understand, for example, the impact of pathologies on blood flows in the cardiovascular system.

In [1] we have proposed a framework for high order (in space and time) fluid structure interaction in 2D using an efficient high order ALE map construction which is described in [2]. In the first part of the presentation, we propose a new high order ALE construction which allows for any type — not only vertical as in [2] — of not too large displacements that applies to 2D as well as 3D. This construction relies on a first order approximation and a correction step that recovers the high order accuracy. In the second part of the talk we present an update of our fluid-structure interaction framework. Along the presentation, we shall display results to illustrate our work.

1 Introduction

Over the last few years, we have been working on building a mathematical and computational framework for high order fluid-structure interaction, see [1, 2, 3, 4, 5, 6], in 2D and 3D, on simplices and hypercubes, with a wide range of applications and in particular, bio-mechanics (e.g. blood flows in arteries). In this paper we present the progress made since our last publications [2, 1] as well as a brief overview of the framework we have built so far.

The paper is organized in the following way: first, we introduce some notations and present a brief overview of the status of [6] in section 1.2 (which will be described in another publication). In section 2 we state our latest advances in one of our central ingredients to achieve high order fluid-structure interaction, namely the Arbitrary Lagrangian-Eulerian framework. Next, the fluid and structure models are presented, associated with their respective discretisation and solution methods. These methods are validated based on the benchmark [7]. In the last section, we propose a fluid-structure interaction solver, combination of the tools presented throughout the paper. The solver is validated by the benchmark [7] and some 3D preliminary results are presented.

1.1 Notations

Given an elementary simplex domain $K^* \subset \mathbb{R}^d$, $d = 1, 2, 3$, and a positive integer N, let us denote by $\mathbb{P}^N(K^*)$ the space of polynomials of total degree less of equal than N, defined in K^*. We fix a reference element, $\hat{K}$, and consider a transformation $\varphi_{K^*} : \hat{K} \longrightarrow K^*$, called the *geometrical transformation*.

We consider now two domains, Ω^* and $\Omega \subset \mathbb{R}^d$, $d = 1, 2, 3$, which we later refer as the *reference* and the *computational* domains, respectively. We further assume that the reference domain has a straight

edge/face mesh associated with it, $\mathcal{T}^*$, ie, $\boldsymbol{\varphi}_{K^*} \in \mathbb{P}^1(\hat{K}), \forall K^* \in \mathcal{T}^*$. Furthermore we admit that the mesh $\mathcal{T}^*$ covers exactly the domain Ω^*, *i.e.*, $\Omega^* = \bigcup_{K^* \in \mathcal{T}^*} \overline{K^*}$.

We denote $P^N_{c,h}(\Omega^*)$, $\boldsymbol{P}^N_{c,h}(\Omega^*)$ the spaces of piecewise scalar, respectively vectorial, polynomial of total degree N, continuous functions in Ω^*, and $P^N_{td,h}(\Omega^*)$ the space of piecewise polynomial of total degree N, totally discontinuous functions in Ω^*.

Finally let us denote by $\boldsymbol{\eta} : \partial\Omega^* \longrightarrow \partial\Omega$ a displacement function. Through $\boldsymbol{\eta}$, we classify three subsets of the boundary: *(i)* Γ^*_M, the portion of the boundary that moves according to the displacement $\boldsymbol{\eta}$, *(ii)* Γ^*_F, the portion of the boundary that stays fixed (ie, $\boldsymbol{\eta}(\boldsymbol{s}) = \boldsymbol{s}, \forall \boldsymbol{s} \in \Gamma^*_F$) and *(iii)* Γ^*_N, the part of the boundary on which we do not prescribe a displacement. The image of each subset, Γ^*_M, Γ^*_F and Γ^*_N by $\boldsymbol{\eta}$ is denoted by Γ_M, Γ_F and Γ_N, respectively. These three sets do not overlap and they verify $\partial\Omega^* = \overline{\Gamma^*_M} \cup \overline{\Gamma^*_F} \cup \overline{\Gamma^*_N}$. Denote $\mathcal{T}^{*,b} = \{K^* \in \mathcal{T}^* : \partial K^* \cap \Gamma^*_M \neq \emptyset\}$ the set of elements K^* sharing a face with the boundary of Ω^*.

1.2 Computational framework for Galerkin methods

Our computational framework builds upon Feel++ [6] which allows for arbitrary order cG and dG Galerkin methods (finite element, spectral elements, ...) in 1D, 2D and 3D on simplices and hypercubes. The computational domain can also be high order, that is to say, the geometrical transformation of each element K of the mesh is a polynomial of degree greater than one. These high order meshes can be generated by Gmsh [8] — up to order five in 2D and order four in 3D. — High order approximations come at a cost both in terms of implementation and computational points of view. The former is addressed by a very generic framework based on modern C++ programming (meta-programming, expression templates, ...) and a language mimicing the mathematical language. The latter is addressed by a careful implementation and optimisation. One of the optimisations that allows to have a huge gain in computational effort is to straighten all the high order elements except for the boundary faces of the computational mesh. This is achieved by moving all the nodes associated to the high order transformation to the position these nodes would have if a first order geometrical transformation were applied. This procedure can be formalized in the following operator

$$\boldsymbol{\eta}_K^{\text{straightening}}(\boldsymbol{\varphi}_K^N(\boldsymbol{x}^*)) = \left(\boldsymbol{\varphi}_K^1(\boldsymbol{x}^*) - \boldsymbol{\varphi}_K^N(\boldsymbol{x}^*)\right) - \left(\boldsymbol{\varphi}_{K\cap\Gamma}^1(\boldsymbol{x}^*) - \boldsymbol{\varphi}_{K\cap\Gamma}^N(\boldsymbol{x}^*)\right) \tag{1}$$

where $\boldsymbol{x}^*$ is any point in K^* and $\boldsymbol{\varphi}_K^1(\boldsymbol{x}^*)$ and $\boldsymbol{\varphi}_K^N(\boldsymbol{x}^*)$ its images by the geometrical transformation of order one and order N, respectively. On one hand, the first two terms ensure that for all K not intersecting Γ, the order one and N transformations produce the same image. On the other hand, the last two terms are 0 unless the image of $\boldsymbol{x}^*$ in on Γ and, in this case, we don't move the high order image of $\boldsymbol{x}^*$. This allows to have straight internal elements and elements touching the boundary to remain high order. When applying numerical integration, specific quadratures are considered when dealing with internal elements or elements sharing a face with the boundary. The performances, thanks to this transformation, are similar to the ones obtained with first order meshes. However, it needs to be used with care as it can generate folded meshes.

2 High order ALE

We now turn to our high order Arbitrary Lagrangian-Eulerian (ALE) framework. A fundamental piece in performing simulations in the ALE framework is the transformation that maps the reference configuration onto the computational domain, at each timestep. This is called *ALE map*. In Pena and Prud'homme [1], the authors propose a high order ALE map that allows for an accurate description of the boundary of the computational domain, while inducing a straight edges in the interior elements of the computational domain's mesh. However, this construction has the disadvantage of relying upon the Gordon-Hall transformations, see Gordon-Hall [9, 10], which makes it (implementation-wise) intrincate to extend to three dimensional domains.

To overcome this difficulty, we replace the stage based on Gordon-Hall transformations, by the solution of a local differential problem in each element in contact with the curved boundary. We review here the construction from [1, 2]. The first step is to perform a modified harmonic extension (according to Masud and Kanchi [11]) of the displacement $\boldsymbol{\eta}$ to the interior of the reference domain using piecewise linear polynomial functions. The corresponding ALE transformation, $\mathcal{A}^1$, satisfies a discrete element-weighted Laplace equation.

The second step is a correction performed in each element that touches the curved boundary in order to build a high order approximation. In each element $K^* \in \mathcal{T}^{*,b}$ we look for $\mathcal{A}^N_{K^*} \in [\mathbb{P}^N(K^*)]^d$ such that

$$\begin{cases} \displaystyle\int_{K^*} (1+\tau)\nabla \mathcal{A}^N_{K^*} : \nabla \mathbf{z}\, dx = 0, & \forall \mathbf{z} \in [\mathbb{P}^N(K^*)]^d \\ \mathcal{A}^N_{K^*}(\boldsymbol{x}^*) = \boldsymbol{\eta}(\boldsymbol{x}^*) + \boldsymbol{x}^* - \mathcal{A}^1(\boldsymbol{x}^*), & \forall \boldsymbol{x}^* \in \partial K^* \cap \Gamma^*_M \\ \mathcal{A}^N_{K^*} = \mathbf{0}, & \text{elsewhere on } \partial K^*. \end{cases}$$

where Γ^*_M is the portion of boundary in the reference domain that is curved in the computational domain. The final ALE map, $\mathcal{A}^N$ is obtained by adding to $\mathcal{A}^1$ the correction $\mathcal{A}^N_{K^*}$ on each element of $\mathcal{T}^{*,b}$

$$\mathcal{A}^N(\mathbf{x}^*) = \mathcal{A}_1(\mathbf{x}^*) + \sum_{K^* \in \mathcal{T}^{*,b}} \mathcal{A}^N_{K^*}(\mathbf{x}^*) + \mathbf{x}^*$$

Proposition 1 (Properties of $\mathcal{A}^N$)**.** *Under the previous assumptions and by construction, $\mathcal{A}^N \in \boldsymbol{P}^N_{c,h}(\mathcal{T}^{*,b})$ — enjoys optimal approximation properties* i.e. *the boundary approximation is $\mathcal{O}\left(h^{N+1}\right)$ in the L_2-norm — and $\mathcal{A}^N \in \boldsymbol{P}^1_{c,h}(\mathcal{T}^* \backslash \mathcal{T}^{*,b})$.*

2.1 The Harmonic extension and Winslow smoother

In both papers [2, 1], the piecewise linear map created in the first step is calculated by performing a harmonic extension (or modified harmonic extension) of the boundary data. However, if the displacement is too large, these operators can induce meshes that are not valid due to, for instance, *mesh folding*. A way to circumvent this problem, that steams from the structure of the proposed ALE map construction, is to replace the harmonic extension by a more suitable and flexible operator that avoids these issues or improves the mesh quality. An example of such an operator is the Winslow smoother [12]. From a continuous point of view, the Winslow smoother enforces that the inverse of the ALE map is harmonic, not the map itself. This accounts for solving a quasi-linear system of PDE's, which can be done using fixed point iterations. In Figure 1 we show the effect of the modified harmonic extension and the Winslow smoother for the same testcase.

2.2 Numerical verification of Proposition 1

We present now some numerical experiments to verify Proposition 1. In order to conduct these experiments we use *(i)* Gmsh [8] to build the initial high order meshes in 2D and 3D and visualize the meshes computed by our methods and *(ii)* Feel++ [6, 3] which provides the framework for arbitrary order Galerkin methods to solve the partial differential equations and handle the computational meshes. Note that the mesh $\mathcal{T}^*$ used to solve equation (1) is built automatically from the initial high order mesh through the straightening process.

We consider the reference domain depicted in Figure 2(a) defined by

$$\Omega^{*,cy} = \left\{ (x^*, y^*, z^*) \in \mathbb{R}^3 : \; x^* \in [0,5]\,, y^{*2} + z^{*2} \leq 0.5^2 \right\} \tag{2}$$

and the associated displacement of its boundary $\boldsymbol{\eta}^{cy}(\boldsymbol{x}^*) = 0.2\, \exp(\frac{x^*}{5}) \sin\left(\frac{\pi x^*}{2.5}\right) \boldsymbol{n}^*$. Figure 2(b) displays the computational domains colored by the corresponding ALE map.

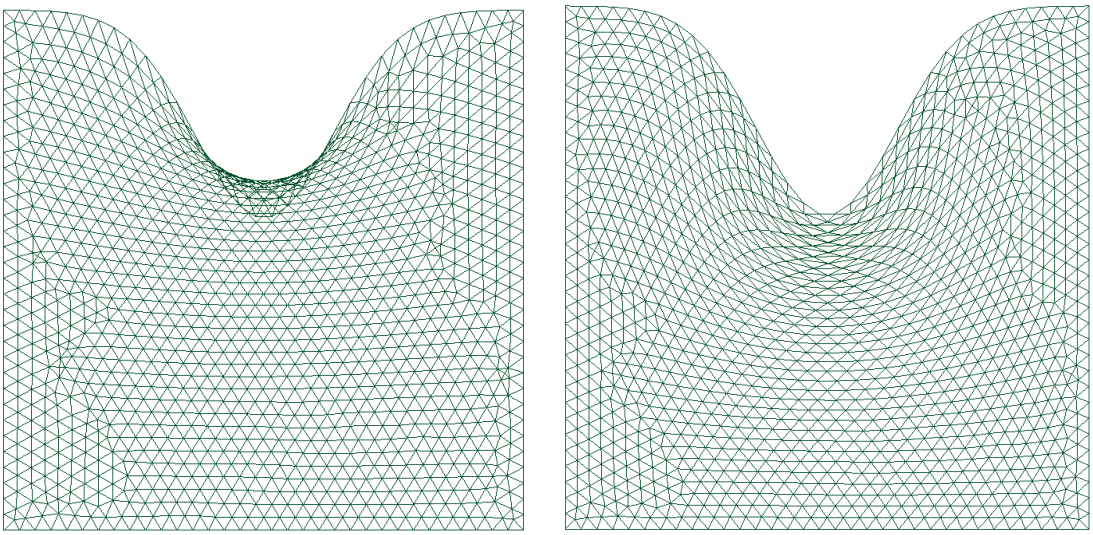

(a) Modified harmonic ALE map

(b) Winslow smoother ALE map

Figure 1: Comparison of first order meshes generated by the harmonic extension (left) and Winslow smoother (right) operators respectively

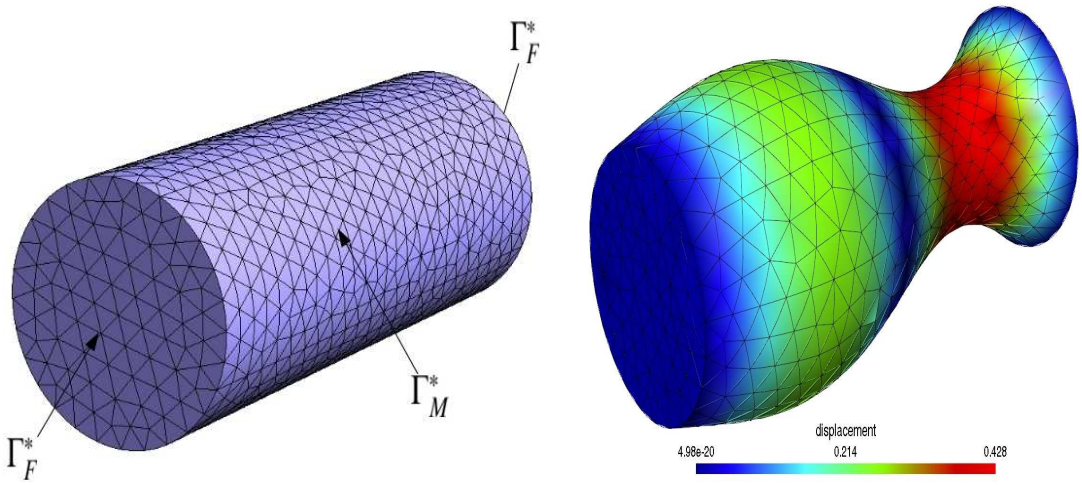

(a) Cylinder, $\Omega^{*,cy}$

(b) Cylinder, $\Omega^{cy} = \mathcal{A}^4(\Omega^{*,cy})$

Figure 2: Reference (left) and computational (right) meshes of order 4 displayed using Gmsh colored by the displacement 2-norm

Finally, Figure 3(a) displays the convergence rate of the quantity $\|\mathcal{A}^N(\boldsymbol{x}^*) - (\boldsymbol{x}^* + \boldsymbol{\eta}(\boldsymbol{x}^*))\|_{[L^2(\Gamma_M^*)]^d}$ which confirms the result of Proposition 1. Figure 3(b) represents the convergence rate with respect to geometric order N.

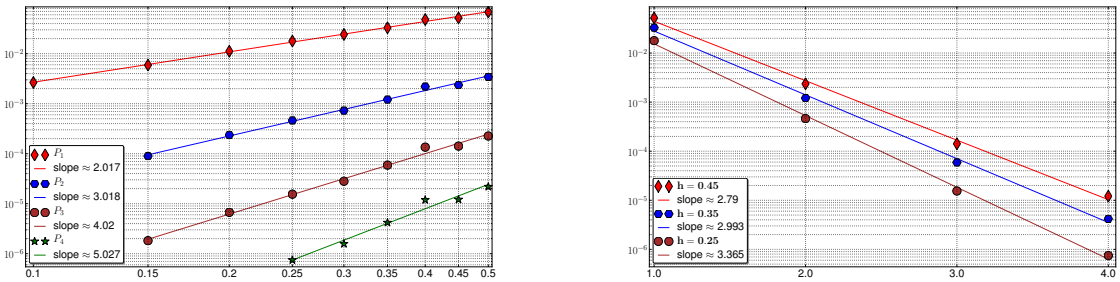

(a) Cylinder

(b) Cylinder

Figure 3: Convergence rate plots of $\mathcal{A}^{N,cy}$ with respect to h (left) and convergence rate plots of $\mathcal{A}^{N,cy}$ with respect to N (right).

3 Models and their discretizations methods

We now turn to the structure and fluid models, their associated discretization and solution methods. In each case, we display some of the results of our strategy applyed to the benchmark [7]. Note that our fluid solver has also been benchmarked for bi-fluid simulations [13] following the proposal [14].

Two benchmarks presented in [7] are performed to verify our code. The first one corresponds to the oscillation of an elastic beam only subjected to gravity. We monitor the coordinates of the tip of the beam. The second is the simulation of a flow in rectangular domain with a rigid obstacle: a flag clamped to a cylinder. We monitor the lift and drag.

The algebraic systems arising from the discretization proposed in the next sections are solved using a Newton or quasi-Newton algorithm with a cubic line search method. At each step, the linear solver applies the GMRES method with a LU preconditioner. The preconditioner is typically built only once throughout the nonlinear iterations unless the nonlinearity is stiff and the preconditioner needs to be recalculated. In the quasi-newton instance, the Jacobian can be rebuilt once in a while during the non-linear iterations or just once, which is often preferred when simulating time-dependent problems. The underlying framework for the linear and nonlinear solvers is PETSc [15].

3.1 Structure

3.1.1 Models and discretizations

We first introduce the deformation gradient tensor, which allows to measure the solid deformation from the displacement $\boldsymbol{\eta}_s$, $\boldsymbol{F}_s = \boldsymbol{I} + \nabla \boldsymbol{\eta}_s$.
Other useful tensors are the right Cauchy-Green tensor $\boldsymbol{C}_s$ and the Green-Lagrange tensor $\boldsymbol{E}_s$ which can be expressed by $\boldsymbol{C}_s = \boldsymbol{F}_s^T \boldsymbol{F}_s, \quad \boldsymbol{E}_s = \frac{1}{2}\left(\boldsymbol{C}_s - I\right)$ where $\boldsymbol{E}_s$ has the property to be divided in two terms, $\boldsymbol{\epsilon_s}$ (linear) and γ_s (quadratic)

$$\boldsymbol{E}_s = \underbrace{\frac{1}{2}\left(\nabla \boldsymbol{\eta}_s + (\nabla \boldsymbol{\eta}_s)^T\right)}_{\boldsymbol{\epsilon_s}} + \underbrace{\frac{1}{2}\left((\nabla \boldsymbol{\eta}_s)^T \nabla \boldsymbol{\eta}_s\right)}_{\gamma_s}. \tag{3}$$

The simplest model of this type is the **elastic linear model**, which is valid for small displacements and deformations. It reads as

$$\rho_s \frac{\partial^2 \boldsymbol{\eta}_s}{\partial t^2} - \nabla \cdot (\boldsymbol{\Sigma}_s) = \boldsymbol{f}_s, \quad \boldsymbol{\Sigma}_s = \lambda_s \left(tr \boldsymbol{\epsilon}_s\right) \boldsymbol{I} + 2\mu_s \boldsymbol{\epsilon}_s \tag{4}$$

with λ_s and μ_s being the Lamé coefficients.

The next model is the **hyper-elastic and compressible model** which is valid for large deformations. The generic balance equation of hyper-elasticity in Lagrangian description is given by

$$\rho_s \frac{\partial^2 \boldsymbol{\eta}_s}{\partial t^2} - \nabla \cdot (\boldsymbol{F}_s \boldsymbol{\Sigma}_s) = \boldsymbol{f}_s, \quad \boldsymbol{\Sigma}_s = \lambda_s \left(tr \boldsymbol{E}_s\right) \boldsymbol{I} + 2\mu_s \boldsymbol{E}_s. \tag{5}$$

where $\boldsymbol{\Sigma}_s$ represents the second Piola-Kirchhoff stress tensor.

To take into account the material incompressibility, we use the **Hyper-elastic and incompressible model**. The pressure p_s acts as a lagrange multiplier to enforce incompressibility. The model reads as

$$\rho_s \frac{\partial^2 \boldsymbol{\eta}_s}{\partial t^2} - \nabla \cdot (\boldsymbol{F}_s \boldsymbol{\Sigma}_s) = \boldsymbol{f}_s, \quad det \boldsymbol{F}_s = 1, \quad \boldsymbol{\Sigma}_s = -p_s (det \boldsymbol{F}_s) \boldsymbol{C}_s^{-1} + \lambda_s \left(tr \boldsymbol{E}_s\right) \boldsymbol{I} + 2\mu_s \boldsymbol{E}_s. \tag{6}$$

Finally we also make use of a **1D reduced model** for thin structures like shells, also known as generalized strings, see [16, 5].

For the numerical results presented in the next section we considered a hyper-elastic model for the structure. We discretized the equations using $[\mathbb{P}^N]^d$ elements and a continuous approximation in space while we used the Newmark method to get an order 2 discretization in time.

3.1.2 Benchmark

The results of the CSM3 benchmark from [7] are displayed in Table 1 and the x, y coordinates of the tip of the beam on the Figure 4. The results are in accordance with the reference values **REF**.

$N_{element}$	N_{dof}	x $[\times 10^{-3}]$	y $[\times 10^{-3}]$
REF		$-14.305 \pm 14.305\,[1.0995]$	$-63.607 \pm 65.160\,[1.0995]$
4199	$17536(P_2)$	$-14.585 \pm 14.59\,[1.0953]$	$-63.981 \pm 65.521\,[1.093]$
4199	$38900(P_3)$	$-14.589 \pm 14.594\,[1.0953]$	$-63.998 \pm 65.522\,[1.093]$
1043	$17422(P_4)$	$-14.591 \pm 14.596\,[1.0953]$	$-64.009 \pm 65.521\,[1.093]$
4199	$68662(P_4)$	$-14.59 \pm 14.595\,[1.0953]$	$-64.003 \pm 65.522\,[1.093]$
4199	$17536(P_2)$	$-14.636 \pm 14.64\,[1.0969]$	$-63.937 \pm 65.761\,[1.0945]$
4199	$38900(P_3)$	$-14.642 \pm 14.646\,[1.0969]$	$-63.949 \pm 65.771\,[1.0945]$
1043	$17422(P_4)$	$-14.645 \pm 14.649\,[1.0961]$	$-63.955 \pm 65.778\,[1.0945]$
4199	$68662(P_4)$	$-14.627 \pm 14.629\,[1.0947]$	$-63.916 \pm 65.739\,[1.0947]$
4199	$17536(P_2)$	$-14.645 \pm 14.645\,[1.0966]$	$-64.083 \pm 65.623\,[1.0951]$
4199	$38900(P_3)$	$-14.649 \pm 14.65\,[1.0966]$	$-64.092 \pm 65.637\,[1.0951]$
1043	$17422(P_4)$	$-14.652 \pm 14.653\,[1.0966]$	$-64.099 \pm 65.645\,[1.0943]$

Table 1: Results for **CSM3** with Δt = 0.02,0.01,0.005. Line **REF** displays the reference values for [7]

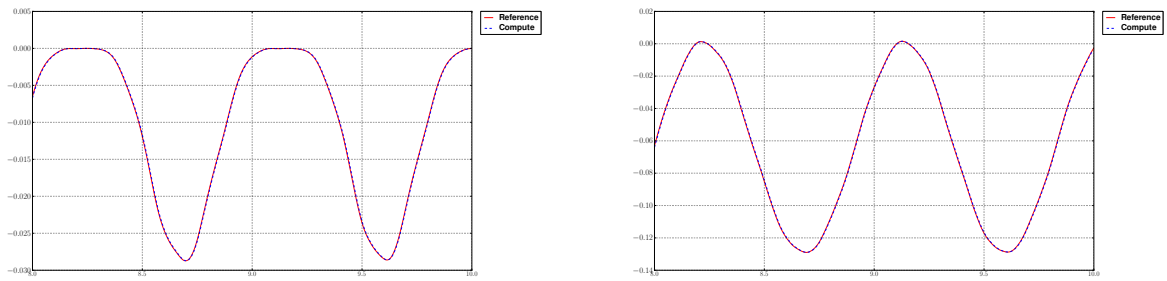

(a) x displacement

(b) y displacement

Figure 4: Results for **CSM3** with Δt = 0.005. x and y displacement of the point A depending on time

3.2 Fluid

3.2.1 Models and discretization

We mainly use a Newtonian fluid model which neglects shear-thining and viscoelastic effects. The govern equations are the classical Navier-Stokes equations which read as

$$\rho_f \frac{\partial \boldsymbol{u}_f}{\partial t} + \rho_f \left(\boldsymbol{u}_f \cdot \nabla\right) \boldsymbol{u}_f - \nabla \cdot \boldsymbol{\sigma}_f = \boldsymbol{f}_f \tag{7}$$

$$\nabla \cdot \boldsymbol{u}_f = 0 \tag{8}$$

where $\boldsymbol{u}_f$ is the fluid velocity and ρ_f its density and

$$\boldsymbol{\sigma}_f = -p_f \boldsymbol{I} + \boldsymbol{\tau}_f, \quad \boldsymbol{\tau}_f = 2\mu_f \boldsymbol{D}_f \ , \ \boldsymbol{D}_f = \frac{1}{2}\left(\nabla \boldsymbol{u}_f + (\nabla \boldsymbol{u}_f)^T\right) \tag{9}$$

where p_f is the pressure and μ_f the fluid viscosity.

The previous equations are discretized using the standard Taylor-Hood element $[\mathbb{P}^N]^d \times \mathbb{P}^{N-1}$ in space and the BDF of order 2 or 3 discretizations in time. In 2D the geometry is discretized using order 1 to 5 geometric transformations while in 3D from order 1 to 4, see [8].

3.2.2 Benchmark

The results of the CFD3 benchmark from [7] are displayed in Table 3.2.2 for various geometrical (N_{geo}) and velocity/pressure $N/N-1$ approximations. The results in Table 3.2.2 for a BDF2 scheme and time step 5×10^{-3} are in accordance with the **REF** results. However, we made some extra computations using a smaller time step $\Delta t = 0.002$ and BDF2/BDF3 schemes and we observe a significant shift in the Drag and Lift coefficients. This shift is already present with BDF3 and $\Delta t = 0.005$. Several computations were made using various meshes and discretization for the velocity, pressure and geometry. BDF2 and BDF3 for $\Delta t = 0.002$ are very much in accordance with the reference results except perhaps for the mean of the Lift which tells us that we are probably resolving properly the time and spatial scales while $\Delta t = 0.005$ using BDF2 or BDF3 is not sufficient.

N_{geo}	$N_{element}$	N_{dof} $(N, N-1)$	N_{bdf}	Drag	Lift
REF				439.45 ± 5.6183 [4.3956]	-11.893 ± 437.81 [4.3956]
P_1	8042	$37514(P_2/P_1)$	2	437.47 ± 5.3750 [4.3457]	-9.7865 ± 437.54 [4.3457]
P_2	2334	$26706(P_3/P_2)$	2	439.27 ± 5.1620 [4.3457]	-8.887 ± 429.06 [4.3457]
P_2	7970	$89790(P_3/P_2)$	2	439.56 ± 5.2335 [4.3457]	-11.719 ± 425.81 [4.3457]
P_1	3509	$39843(P_3/P_2)$	2	438.24 ± 5.5375 [4.3945]	-11.024 ± 433.90 [4.3945]
P_1	8042	$90582(P_3/P_2)$	2	439.25 ± 5.6130 [4.3945]	-10.988 ± 437.70 [4.3945]
P_2	2334	$26706(P_3/P_2)$	2	439.49 ± 5.5985 [4.3945]	-10.534 ± 441.02 [4.3945]
P_2	7970	$89790(P_3/P_2)$	2	439.71 ± 5.6410 [4.3945]	-11.375 ± 438.37 [4.3945]
P_3	3499	$73440(P_4/P_3)$	3	439.93 ± 5.8072 [*4.4921*]	-14.511 ± 440.96 [4.3945]
P_4	2314	$78168(P_5/P_4)$	2	439.66 ± 5.6412 [4.3945]	-11.329 ± 438.93 [4.3945]
P_3	2340	$49389(P_4/P_3)$	2	440.03 ± 5.7321 [4.3945]	-13.25 ± 439.64 [4.3945]
P_3	2334	$49266(P_4/P_3)$	3	440.06 ± 5.7773 [4.3945]	-14.092 ± 440.07 [4.3945]

Table 2: Results for **CFD3** with Δt = 0.01,0.005,0.002. Line **REF** displays the reference values for [7]

4 Fluid structure interaction

In the fluid-structure interaction context, we chose to write the fluid dynamics equations in the *Arbitrary Lagrangian Eulerian* (ALE) framework. It allows to take into account the deformation of the fluid

domain. We need also to introduce into our model the domain's velocity of deformation $\boldsymbol{w}_f$, see e.g. [1, 2], the fluid equation set now reads in the moving domain Ω_t over the time interval I:

$$\rho_f \left.\frac{\partial \mathbf{u}_f}{\partial t}\right|_{\mathbf{x}^*} - \mathbf{div}_{\mathbf{x}}(2\mu_f \mathbf{D}_{\mathbf{x}}(\mathbf{u}_f)) + \rho_f((\mathbf{u}_f - \mathbf{w}_f)\cdot \boldsymbol{\nabla}_{\mathbf{x}})\mathbf{u}_f + \nabla_{\mathbf{x}} p_f = \mathbf{f}, \quad \text{in } \Omega_t \times I \tag{10}$$

$$\mathrm{div}_{\mathbf{x}}(\mathbf{u}_f) = 0, \quad \text{in } \Omega_t \times I \tag{11}$$

where all differential operators are defined w.r.t. the Eulerian coordinate system, except the ALE time derivative.

The fluid and the structure are coupled through a partitioned method with an implicit or semi-implicit scheme, see [1, 5] for more details.

4.1 2D Benchmark

This final benchmark is a mix of the two previous tests. We remove the gravity and the flag part (not the cylinder) is now allowed to move. The results are in accordance with the reference values even though we used a really coarse mesh except for the drag. A complete study using high order approximation like for the fluid shall be available at the time of Acomen'11.

	x $[\times 10^{-3}]$	y $[\times 10^{-3}]$	Drag	Lift
REF	$-2.69 \pm 2.53\,[10.9]$	$1.48 \pm 34.38\,[5.3]$	$457.3 \pm 22.66\,[10.9]$	$2.22 \pm 149.78\,[5.3]$
	$-2.85 \pm 2.73\,[10.7]$	$1.68 \pm 33.93\,[5.4]$	$435.5 \pm 28.93\,[10.7]$	$-13.45 \pm 178.73\,[5.4]$

Table 3: Results for **FSI3** with Δt = 0.01. There are 4414 elements in Ω_f and 20653 dofs associated (P_2/P_1), 396 elements in Ω_s and 1794 dofs associated (P_2). The geometry is first order and the BDF scheme for the fluid is order 2. **REF** values are found in [7]

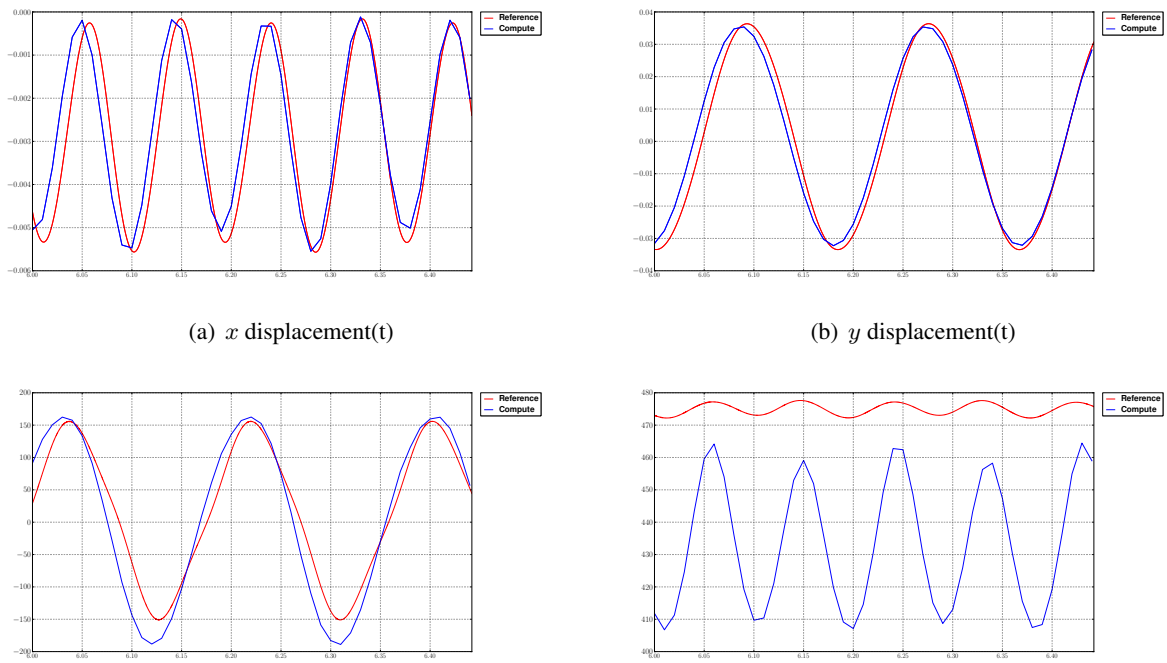

(a) x displacement(t)

(b) y displacement(t)

(c) Lift(t)

(d) Drag(t)

Figure 5: Results for **FSI3** with Δt = 0.01.

4.2 3D Benchmark

Finally we present a blood flow application in large arteries that has been proposed in [16]. The geometry is a straight pipe and a pressure pulse of $1.3332 \times 10^4 g/\left(cm\ s^2\right)$ has been imposed at the inlet boundary during $0.003s$. The thin elastic vessel $(0.1cm)$ is clamped at the inlet and outlet. Figure 6 shows the pressure wave propagation for different time steps. We have used a (P_2/P_1) space for the fluid and P_1 for the structure. The geometry for the fluid and structure is order one. The time scheme for the fluid is also order 1.

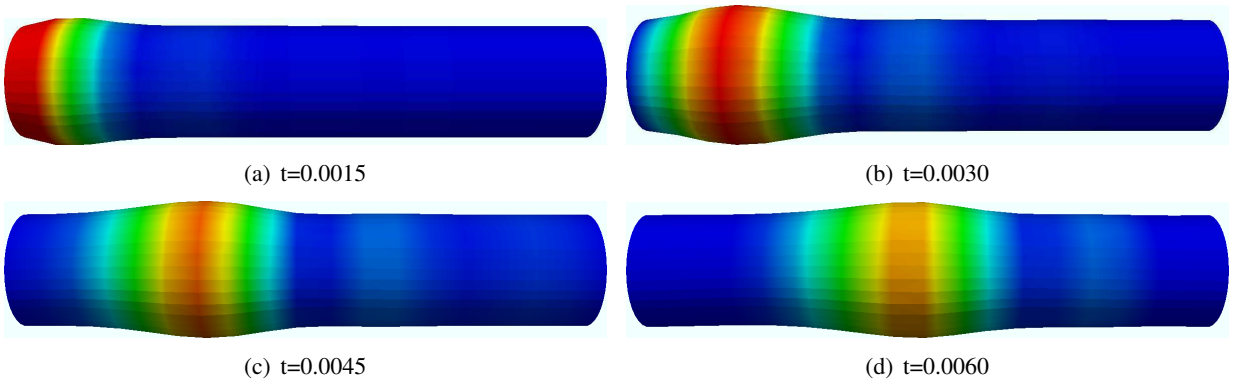

(a) t=0.0015 (b) t=0.0030

(c) t=0.0045 (d) t=0.0060

Figure 6: Pressure wave in a straight pipe. We show the fluid pressure and the fluid displacement of the pipe is magnified 15 times.

5 Conclusion

Some of the results in this paper are very recent, not fully exploited or complete. In particular we do not yet display results for high order fluid structure interaction in 3D including geometry although the main components of the FSI framework namely the structure and flow solver as well as ALE framework enjoy optimal properties when using high order approximations separately. Complete results will be available at the time of Acomen'11.

Acknowledgments

This work is funded by the Région Rhône-Alpes (ISLE/CHPID project), the ANR (MOSICOB project) and Calouste Gulbenkian Foundation (*Estímulo à Investigação* project).

References

[1] Gonçalo Pena and Christophe Prud'homme. Construction of a high order fluid-structure interaction solver. *J. Comput. Appl. Math.*, 234(7):2358–2365, August 2010.

[2] Christophe Prud'homme, Gonçalo Pena, and Alfio Quarteroni. High order methods for the approximation of the incompressible Navier-Stokes equations in a moving domain. *Comput. Meth. Appl. Mech. Eng.*, 2011. to appear.

[3] Christophe Prud'homme. Life: Overview of a unified C++ implementation of the finite and spectral element methods in 1d, 2d and 3d. 2007.

[4] Christophe Prud'homme. A domain specific embedded language in C++ for automatic differentiation, projection, integration and variational formulations. 2006.

[5] G. Pena. *Spectral element approximation of the incompressible Navier-Stokes equations evolving in a moving domain and applications*. PhD thesis, École Polytechnique Fédérale de Lausanne, November 2009. n°4529.

[6] C. Prud'homme, V. Chabannes, and G. Pena. Feel++: Finite Element Embedded Language in C++. Free Software available at http://www.feelpp.org. Contributions from A. Samake, V. Doyeux, M. Ismail and S. Veys.

[7] S. Turek and J. Hron. Proposal for numerical benchmarking of fluid-structure interaction between an elastic object and laminar incompressible flow. *Fluid-Structure Interaction*, pages 371–385, 2006.

[8] C. Geuzaine and J.-F. Remacle. Gmsh: a three-dimensional finite element mesh generator with built-in pre-and post-processing facilities. *International Journal for Numerical Methods in Engineering*, 79(11):1309–1331, 2009.

[9] W. J. Gordon and C. A. Hall. Construction of curvilinear coordinate systems and their applications. *Int. J. Numer. Meth. Eng.*, 7:461–477, 1973.

[10] W. J. Gordon and C. A. Hall. Transfinite element methods: blending-function interpolation over arbitrary curved element domains. *Int. J. Numer. Meth. Eng.*, 21:109–129, 1973.

[11] H. Kanchi and A. Masud. A 3D adaptive mesh moving scheme. *International Journal for Numerical Methods in Fluids*, 54(6-8):923–944, 2007.

[12] A. Winslow. Numerical solution of the quasilinear poisson equations in a nonuniform triangle mesh. *J. Comp. Phys.*, 2:149–172, 1967.

[13] V. Doyeux, Y. Guyot, V. Chabannes, C.Prud'homme, and M. Ismail. Simulation of two phase flow using a level set method. application to vesicle dynamics. In *Fifth International Conference on Advanced COmputational Methods in ENgineering (ACOMEN 2011)*, 2011.

[14] S. Hysing, S. Turek, D. Kuzmin, N. Parolini, E. Burman, S. Ganesan, and L. Tobiska. Quantitative benchmark computations of two-dimensional bubble dynamics. *International Journal for Numerical Methods in Fluids*, 60(11):1259–1288, 2009.

[15] Satish Balay, William D. Gropp, Lois Curfman McInnes, and Barry F. Smith. Efficient management of parallelism in object oriented numerical software libraries. In E. Arge, A. M. Bruaset, and H. P. Langtangen, editors, *Modern Software Tools in Scientific Computing*, pages 163–202. Birkhäuser Press, 1997.

[16] F. Nobile. Numerical approximation of fluid-structure interaction problems with application to haemodynamics. *PhD, Ecole Polytechnique Féderale de Lausanne, Switzerland*, 2001.